Synthesis and design of $NaNi_{1/3}Fe_{1/3}Mn_{1/3}O_2$ cathode materials for long-life sodium-ion batteries

Song, Tengfei; Zhang, Qiyao; Chen, Yongxiu; Zhu, Pengcheng; Kendrick, Emma

DOI:
10.1016/j.ceja.2023.100572

Document Version
Version created as part of publication process; publisher's layout; not normally made publicly available

Citation for published version (Harvard):
Song, T, Zhang, Q, Chen, Y, Zhu, P & Kendrick, E 2023, 'Synthesis and design of $NaNi_{1/3}Fe_{1/3}Mn_{1/3}O_2$ cathode materials for long-life sodium-ion batteries', *Chemical Engineering Journal Advances*. https://doi.org/10.1016/j.ceja.2023.100572

Synthesis and design of $NaNi_{1/3}Fe_{1/3}Mn_{1/3}O_2$ cathode materials for long-life sodium-ion batteries

Tengfei Song , Qiyao Zhang , Yongxiu Chen , Pengcheng Zhu , Emma Kendrick

PII: S2666-8211(23)00129-1
DOI: https://doi.org/10.1016/j.ceja.2023.100572
Reference: CEJA 100572

To appear in: *Chemical Engineering Journal Advances*

Received date: 23 June 2023
Revised date: 26 October 2023
Accepted date: 4 November 2023

Please cite this article as: Tengfei Song , Qiyao Zhang , Yongxiu Chen , Pengcheng Zhu , Emma Kendrick , Synthesis and design of $NaNi_{1/3}Fe_{1/3}Mn_{1/3}O_2$ cathode materials for long-life sodium-ion batteries, *Chemical Engineering Journal Advances* (2023), doi: https://doi.org/10.1016/j.ceja.2023.100572

Highlights

- Regression equations derived for synthesis conditions and physical and electrochemical properties, including cycle-life.
- Higher pH yields larger D50, higher tap density, but decreases crystallite size and uniformity, affecting cycling.
- Increased NH_4OH concentration improves uniformity and tap density of particles.
- Stirring speed affects crystallite size, and interaction effects of pH with NH_4OH or stirring speed impact cycling.
- Validation experiment produces uniform particles, tap density of 1.50 g cm^{-3} and threefold increase in cycle life.

Synthesis and design of $NaNi_{1/3}Fe_{1/3}Mn_{1/3}O_2$ cathode materials for long-life sodium-ion batteries

Tengfei Song [1]*, Qiyao Zhang[1], Yongxiu Chen[1], Pengcheng Zhu[2], Emma Kendrick [1,]*

1 School of Metallurgy and Materials, University of Birmingham, Birmingham B15 2TT, U.K
2 School of Chemistry, University of Birmingham, Edgbaston, Birmingham, B15 2TT, UK.

Graphical Abstract

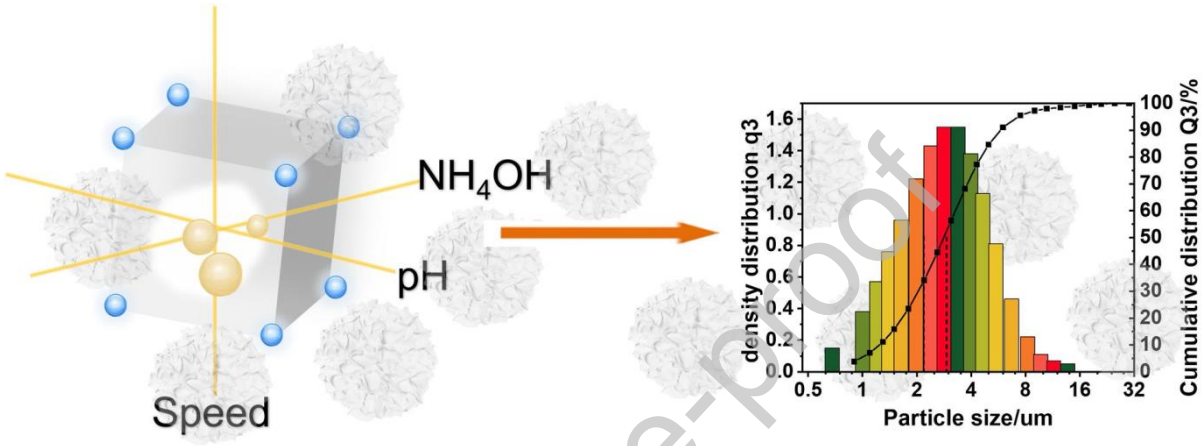

Keywords: Sodium-ion Batteries, Cathode, Synthetic Conditions, Design of Experiments, Analysis of Variance (ANOVA)

Abstract: To enable the widespread adoption of residential energy storage, sustainable, low-cost, long-life, and energy-dense battery technologies are required. Sodium-ion offers many of these characteristics, however often the system is tailored for energy rather than cycle life. In this work, the effect of synthesis conditions upon the primary and agglomerated secondary particle size and shape of the sodium-ion cathode material $NaNi_{1/3}Fe_{1/3}Mn_{1/3}O_2$ was investigated for optimization of energy and cycle life. A two-level full factorial experimental design was utilized to examine how the synthesis parameters (pH, molar ratio of ammonia/metal precursor salt, and stirring speed) affect the physical and electrochemical properties. This approach enabled a comprehensive investigation of the main effects and interactions of these parameters. The data from multiple synthesis runs were analyzed using statistical methods and regression analysis. This experimental design provided valuable insights into the relationship between synthesis parameters and material properties. Statistical analysis indicates that both physical and electrochemical properties are mainly controlled through pH and NH_4OH, while the effects of stirring speed are less pronounced. The optimal synthetic conditions producing the highest cycling performance were extrapolated from the statistical analysis. A validation experiment showed that particles synthesized with optimum parameters displayed a threefold increase in cycling performance together with uniformly distributed particle size and a high tap density.

1. INTRODUCTION

Lithium-ion batteries (LIBs) are a mature electrochemical energy storage technology and have been incorporated into a diverse array of applications since its commercialization by Sony in the 1990s. However, the relatively low abundance and non-uniform global distribution of lithium (Li), cobalt (Co) and more recently nickel (Ni) resources have raised concerns about the sustainable supply to meet the future market demand[1-4], especially with the dramatic increase in the number of

electric vehicles and stationary energy storage devices needed to reach the targeted Net Zero by 2050[5]. Sodium metal batteries such as the NAS (Sodium–sulfur) and Zebra (sodium–metal-halide) batteries have been considered for stationary storage applications for some time, [9] however more recently sodium-ion as a replacement for Li-ion have been considered. Sodium-ion batteries (NIBs) offer a low-cost sustainable alternative to current LIBs[6, 7]. Their sustainability arises from the reduction in the use of critical elements and strategic materials, and potential long life, however, the economics for recycling are still being discussed.[8] To maximize their potential for stationary energy storage, new cathode materials with high energy densities and stable structures are required which give longer cycle life. [10, 11] Several chemistries have been investigated including Layered oxide cathode systems[12, 13] and Prussian White or Blue analogues[14]. Cobalt-free O3-type layered $NaNi_{1/3}Fe_{1/3}Mn_{1/3}O_2$ is one of the most promising cathode materials for NIBs because of its high theoretical capacity, good reversibility, usage of abundant raw materials, and flexible synthesis process[15]. Several methods have been reported in the synthesis of NaNFM cathode including solid-state[16, 17], oxalate coprecipitation[18], and hydroxide coprecipitation methods[19-21]. However, to our knowledge, few studies have systematically investigated the impacts of synthesis conditions on the particle physical properties and effects upon electrochemical performance.

Hydroxide co-precipitation is widely used in industry for the synthesis of cathode materials due to its intimate mixing of the precursor ionic components. The synthesis process involves the precipitation of metal hydroxides from a salt solution, and the subsequent formation, growth, and maturation of these particles, as well as agglomeration and fragmentation in the reactor. The properties of synthesized metal hydroxide ($TM(OH)_2$), such as morphology, size distribution, and tap density are significantly dependent on synthetic conditions. This is attributed to the complex competition between precipitation and complexation reactions as well as many conjugated input parameters; including temperature, pH, stirring speed, feeding concentration, feeding rate, residence time, and amount of chelating agent [22]. The precursor hydroxide particles are then milled and mixed with the alkali hydroxide or carbonate and fired. The control of the co-precipitation variables is critical to optimize the properties of the hydroxide intermediate products and the resulting fired active material, which ultimately affects the final performance properties of the cells. A detailed understanding of how process variables affect the physical and electrochemical properties is critical to designing materials with the desired characteristics.

Considerable efforts have been dedicated to enhancing the synthesis conditions with the goal of achieving uniformly dispersed spherical particles in lithium-ion batteries. For example, Lee *et al*.[23] conducted a study to determine the optimal conditions for producing spherical $(Ni_{1/3}Co_{1/3}Mn_{1/3})(OH)_2$ by controlling factors such as pH, stirring speed, and the quantity of chelating agent. Noh *et al*.[24] optimized the process conditions of $Ni_{0.6}Co_{0.2}Mn_{0.2}(OH)_2$ precursor, aiming to improve their performance at high rates and elevated temperatures. Liang *et al*.[22] focused on optimizing the process conditions for high tap-density and morphology of $Ni_{0.6}Co_{0.2}Mn_{0.2}(OH)_2$ precursor. Dense and spherical hydroxides with a tap density of 1.94 g cm^{-3} were obtained. However, these endeavors were predominantly conducted through time-consuming trial and error or single-factor experiments (OFAT), which not only fail to identify the crucial factors influencing the output results but also risk overlooking the optimal settings for these factors.

To streamline the optimization process for new materials, there have been attempts to quantify the impact of synthesis variables on the desired outcome. Barai *et al*. [25] developed a comprehensive multi-scale computational model to simulate particle evolution during the co-precipitation process. This model enables the prediction of final particle size and size distribution based upon pH and

ammonia content. Similarly, Para *et al*.[26], conducted a trial where they employed a population balance model to simulate the initial stages of particle formation during co-precipitation. However, constructing and validating these models requires substantial data and experiments to minimize discrepancies between experimental and simulated values and advanced statistics is necessary for accurate simulations.

In the existing literature, there has been a lack of emphasis on applying the Design of Experiments (DoE) methodology for the investigation and optimization of battery material synthesis. DoE is an effective problem-solving approach that allows for the identification of key factors and their effects by conducting a minimal number of experiments with multiple variable parameters. It enables simultaneous adjustments of multiple factors to be made. Aside from discerning the primary factor effects, DoE can also facilitate the detection of interactions among these factors and provide statistical models to predict output results.

In this work, the Design of Experiments (DoE) methodology is used, for the first time, in the synthesis of $NaNi_{1/3}Fe_{1/3}Mn_{1/3}O_2$, specifically aiming to establish the relationship between input variables and the outcome of the precursor preparation step. Based on prior knowledge, the pH level, chelating agent quantity, and stirring rate were recognized as key factors which influence the physicochemical properties of both intermediate and final powders [22]. Experimental procedures were conducted in a 5 L reactor, and the physical and electrochemical properties of the obtained samples were characterized to ascertain the impact of synthesis conditions, and, ultimately to identify the optimal synthesis parameters. Minitab Statistical Software was employed to facilitate the experimental design and data analysis processes. The effects of the input variables on the output response were assessed and an optimized synthesis condition proposed. An improved understanding of how the synthesis conditions influence particle properties and ultimate electrochemical performance is also discussed.

The objectives of this study are:

(1) To establish a systematic engineering research methodology for identifying the critical parameters for optimizing the co-precipitation process to maximize performance. The outcomes of this study will provide a statistical model for predicting synthesis parameters to produce uniformly distributed particles. The goal is to minimize surface side reactions, enhance tap density, and prolong lifetime.
(2) To establish a connection between the synthesis parameters and the morphology as well as the electrochemical properties.

2. EXPERIMENTAL AND METHODS

2.1 Experimental design and analysis

In this study, three synthesis factors, pH, the molar ratio of NH_4OH /$TMSO_4$(TM=Ni, Fe, Mn), and stirring speed (rpm) are selected as the input variables with a low and high level based on a 2^k (level factor) full factorial design matrix. To assess the curvature of the fitted model, three additional replications of the central points (current parameters) were included. The temperature, metal sulfate and alkali concentration, metal sulfate feed flow rate, and residence time were held constant at optimal values determined from previous experiments across the DoE matrix. As a result, a design matrix consisting of a total of 11 experiments was generated using Minitab, as depicted in Figure 1 and Table 1.

The various responses of interest in this study include morphology, tap density (g/cm^3), particle size (um), particle distribution, structural properties, crystallite size, initial formation capacity ($mAh\ g^{-1}$)

and cycling performance. Particle distribution was quantified as (D90 – D10)/D50 while the crystal structural was represented by the x-ray diffraction peak intensity ratio I003/I104, a commonly used indicator of cation mixing degree[27, 28]. The capacity retention after cycling under 0.5 C for 50 cycles was selected as the major output response.

The contribution of individual factors and their interactions to the response is evaluated by the ANOVA (Analysis of variance). The confidence level was set to 95% (α=0.05), corresponding to probability values (hereafter p-value) < 0.05. The p-value (probability value) was used to determine whether a factor or interaction is significant or not during the data fitting process. Specifically, factors with a p-value greater than 0.05 were considered statistically insignificant and were excluded from the regression model. The regression model considers both liner (Eq.1) and second-order polynomial (Eq.2) relationships between input factors (x_i, $i=1,2,3$) and output response (Y) depends on the quality of the fitting:

$$Y = \beta_0 + \sum_{i=1}^{3} \beta_i x_i + \sum\sum_{i<j}^{3} \beta_{ij} x_i x_j \quad (1)$$

$$Y = \beta_0 + \sum_{i=1}^{3} \beta_i x_i + \sum_{i=1}^{3} \beta_{ii} x_i^2 + \sum\sum_{i<j}^{3} \beta_{ij} x_i x_j \quad (2)$$

Where β_0 is the constant, $\beta_i, \beta_{ij}, \beta_{ii}$ are the regression coefficients of linear effect, 2-Way interactive effect, and quadratic effect, respectively.

Correlation coefficient (R^2) and predicted R^2 (R^2_{pred}) obtained from ANOVA were used as accuracy metrics to describe the reliability of fit and predictive capabilities of the regression models. The closer R^2 to 1 refers to a better fit and prediction performance.

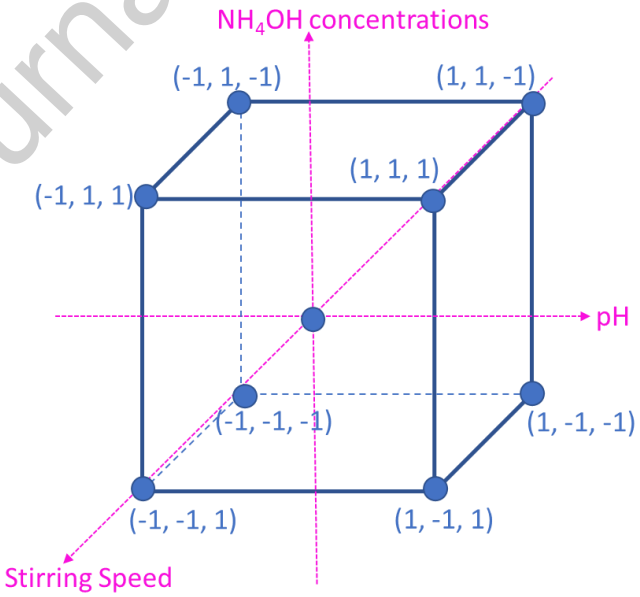

Figure 1 Design matrix with three operating conditions

Table 1 Experimental design matrix for the $Ni_{1/3}Fe_{1/3}Mn_{1/3}(OH)_2$ co-precipitation reactions with different pH, ammonium hydroxide quantity and stirring speed.

DOE No.	Uncoded	Coded

	x_1 pH	x_2 NH_4OH/TM	x_3 Stirring speed (rpm)	x_1 pH	x_2 NH_4OH/TM	x_3 Stirring speed (rpm)
1	10.0	0.8	400	-1	-1	-1
2	11.0	0.8	400	1	-1	-1
3	10.0	1.2	400	-1	1	-1
4	11.0	1.2	400	1	1	-1
5	10.0	0.8	800	-1	-1	1
6	11.0	0.8	800	1	-1	1
7	10.0	1.2	800	-1	1	1
8	11.0	1.2	800	1	1	1
9	10.5	1.0	600	0	0	0
10	10.5	1.0	600	0	0	0
11	10.5	1.0	600	0	0	0

Note: The design as shown is a non-randomised design (standard order). Central points are mixed with the other runs so that the Center Points are true "replicates" thus adding degrees of freedom.

2.2 Material synthesis

The synthesis process involves the reaction of a well-mixed metal salt solution with a precipitating agent and chelating agent to obtain the precursor, which is then subjected to high temperature sintering with a specific quantity of sodium salt to produce the final product. 2L of deionized water is added to a 5L stirred tank reactor and heated to 50 °C under N_2 protection. In parallel, a 2 M (1L) mixed metal aqueous solution consisting of $NiSO_4{\cdot}6H_2O$, $FeSO_4{\cdot}7H_2O$, and $MnSO_4{\cdot}H_2O$ (molar ratio of Ni^{2+}: Fe^{2+}: Mn^{2+} =1: 1: 1) and 1 L of the NaOH:NH_4OH mixture is pumped into the stirred tank at 1 mL min^{-1}. Stirring is performed at various rpm with a four-finned baffle. The pH is carefully controlled to the required value by adjusting the NaOH pumping rate. After vigorous stirring for 24 h, the precipitate is filtered and rinsed thoroughly with deionized water, followed by dried in a vacuum oven at 120 °C overnight. The obtained precursor $Ni_{1/3}Fe_{1/3}Mn_{1/3}(OH)_2$ is calcined with Na_2CO_3 at 900 °C for 9 h at a heating rate of 2 °C min^{-1} to obtain a layered $NaNi_{1/3}Fe_{1/3}Mn_{1/3}O_2$ cathode material. A schematic diagram depicting the process is illustrated in Figure 2.

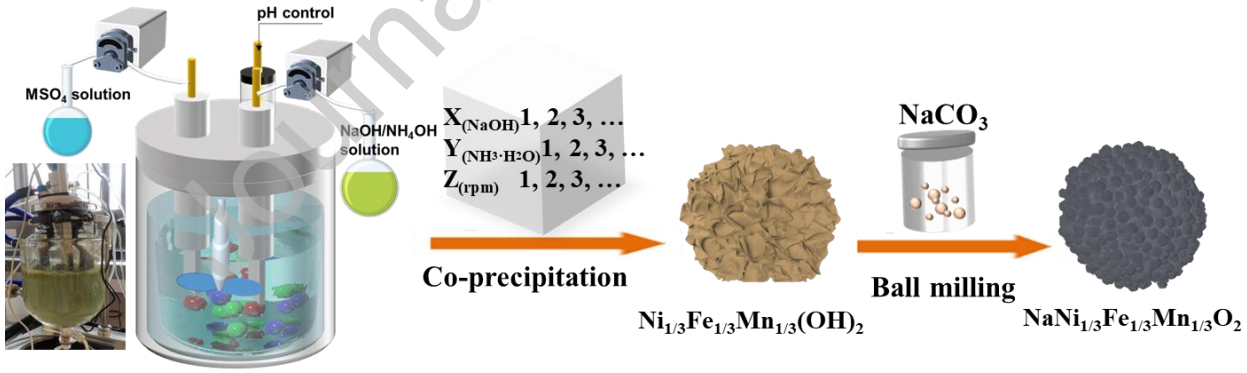

Figure 2. Illustration of the synthesis and optimization process.

2.3 Analytical techniques

The structural characteristics of the as-prepared powder materials is examined by X-ray diffraction (XRD, Proto, Cu Kα, λ = 1.54056 Å). The data is recorded at a degree step of 0.03° between 10-100° at 30 KV and 20 mA, and Rietveld refinement performed using GSAS-I to acquire lattice parameters. Scanning electron microscopy (SEM, Zeiss EVO15) operated at 10 KV, 15 pA, was performed to investigate particle morphology. Tap densities are measured using an autotap analyzer (Quantachrome) with 1000 times vibration. A laser particle size analyzer (Sympatec, HELOS) with a wavelength of 635 nm is used to examine the particle size and distribution of the final powders. Each sample is measured three times and averaged.

2.4 Electrochemical performance tests

The electrochemical characterizations are evaluated in CR2032 coin-type half-cells assembled in an argon-filled glove box, comprising a cathode, Na metal anode (Aldrich, 99%), separator (Glass fiber), and 1 M NaPF6 in EC: DEC: FEC (12.6: 47.1: 35: 5.3 wt%). The cathodes are prepared by mixing the active material, carbon black (TimCal, C65), CNT, oxalic acid additive, and PVDF binder in a mass ratio of 87.0: 5.8: 0.2: 1.0: 6.0 in NMP solvent using a THINKY Mixer. The well-mixed slurry is then coated onto an aluminum foil with a Doctor blade and dried at 120℃ for 24 hours in a vacuum oven. The mass loading of active materials on the cathodes is 6~7 mg cm^{-2}. The cells are galvanostatically cycled at C/2 CC-CV (C/20 current cut off limit) charge and C/2 discharge on a BCS battery test system within the voltage range of 2.0-4.1 V vs Na^+/Na at room temperature. Prior to cycling, three formation cycles at C/10 CC-CV (C/50 current cut off limit) charge and C/10 discharge are conducted to check the formation capacity. Three repeats of each cell are performed.

3. RESULTS AND DISCUSSION

3.1 Physical properties

A series of eleven syntheses were performed, each synthesis, including washing, filtering, drying, firing, and processing, takes approximately one week to complete. The obtained powders are handled and processed exclusively in glove box conditions to minimize any surface degradation of the materials, and the physical attributes of the materials are compared. A summary of the key results is provided in Table 2.

Table 2 Summary of experimental design and measured physical response results.

DOE No.	Synthesis conditions			Response				
	pH	NH_4OH/ TM	Stirring speed (rpm)	Particle size D50 (um)	Size distribution	Tap density (g/cm^3)	Crystallite size (nm)	I003/I104
1	10.0	0.8	400	2.00	1.71	0.98	53.894	0.82
2	11.0	0.8	400	3.18	2.14	1.10	49.002	0.88
3	10.0	1.2	400	2.42	1.73	1.17	61.798	0.90
4	11.0	1.2	400	11.43	3.13	1.38	57.546	0.73
5	10.0	0.8	800	1.68	1.57	1.08	42.467	1.03
6	11.0	0.8	800	3.06	1.80	1.15	39.305	1.02
7	10.0	1.2	800	2.76	1.49	1.29	46.120	1.07
8	11.0	1.2	800	12.64	2.47	1.55	45.160	1.03
9	10.5	1.0	600	2.14	1.79	1.13	51.974	0.87
10	10.5	1.0	600	2.06	1.67	1.21	55.898	0.92
11	10.5	1.0	600	2.43	1.54	1.26	51.070	0.85

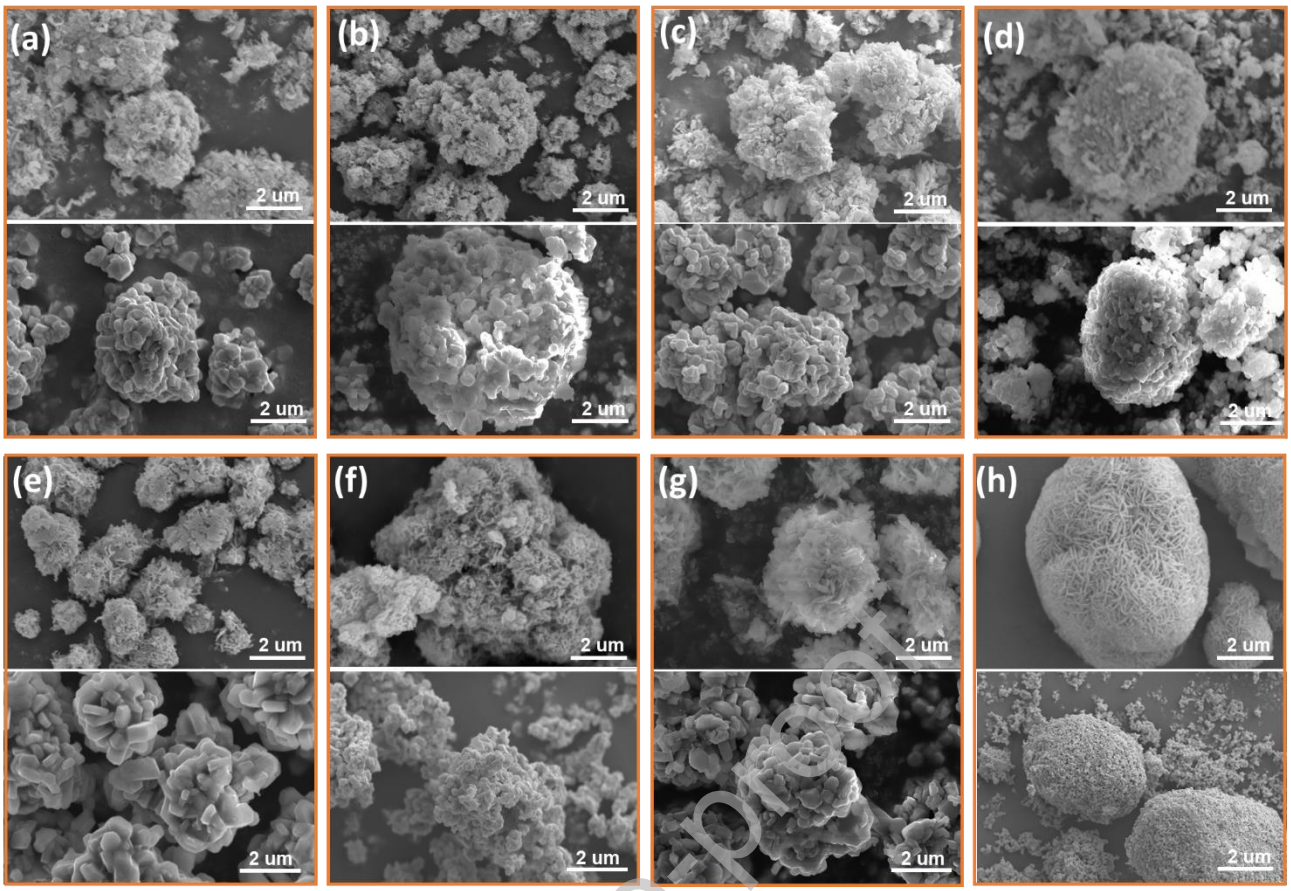

Figure 3. SEM images of the as-prepared hydroxide precursors (top) and final layered oxide particles (bottom) prepared at DoE1 (a), DoE2 (b), DoE3 (c), DoE4 (d), DoE5 (e), DoE6 (f), DoE7 (g), and DoE8 (h).

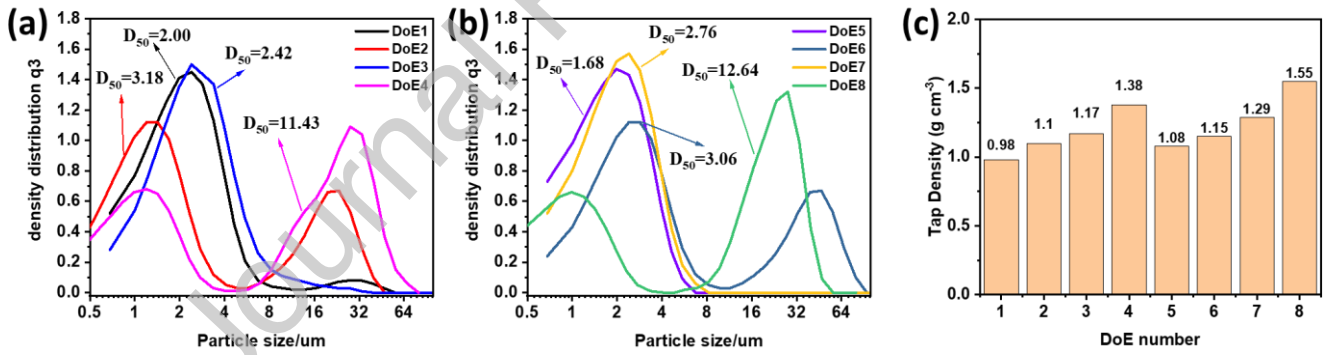

Figure 4. Particle size distribution (a,b) and tap density (c) of the synthesized final particles.

Figure 3 displays the SEM images of the synthesized layered oxide NaNFMO particles and their corresponding precursors. For clear comparison, the particle size distributions and tap density values of the final particles are shown in Figure 4. When the pH is set to 10, the obtained precursors exhibit a lamellar-like morphology (Figure 3a, c, e, g). After sodiation, the secondary particles undergo a transformation into quasi-spherical morphologies composed of randomly stacked primary particles with an average diameter of around 400 nm. In contrast, when the pH is increased to 11, the precursors adopt a needle-like shape (Figure 3b, d, f, h), and the size of the primary particles reduces to approximately 200 nm after sodiation. Moreover, at higher pH values, the particle morphology becomes less uniform, and significant agglomeration with numerous fine particles can be observed. This is also reflected in the particle size distribution diagram, where two peaks are evident (Figure 4a, b). These small and immature grains may originate from the direct formation of hydroxide precipitates without coordination with ammonia during the initial stages in a strong alkali environment. The irregular morphology and broad particle size distribution at high

pH values are unfavourable for rapid Na^+ diffusion processes and are expected to exacerbate side reactions between particles and electrolyte, leading to accelerated capacity loss during cycling. In addition, samples synthesized at high pH tend to exhibit higher tap densities (Figure 4c). This can be attributed to the fact that smaller particles can fill the voids among larger ones when mixing particles with different sizes.

The concentration of NH_4OH also plays a crucial role in determining the properties of the particles. Previous studies have demonstrated that a higher concentration of NH_4OH is advantageous for achieving densely packed secondary particles [23, 29]. Figure 3 illustrates that, with increased NH_4OH concentration, the secondary particles exhibit a more spherical shape with densely packed primary grains. Additionally, it is evident that the secondary particles grow, as indicated by the increase in D50 values from 1.68 to 2.76 µm and 3.06 to 12.64 µm for DoE 5-8. To provide a visual representation of this process, a schematic illustration is presented in Figure 5.

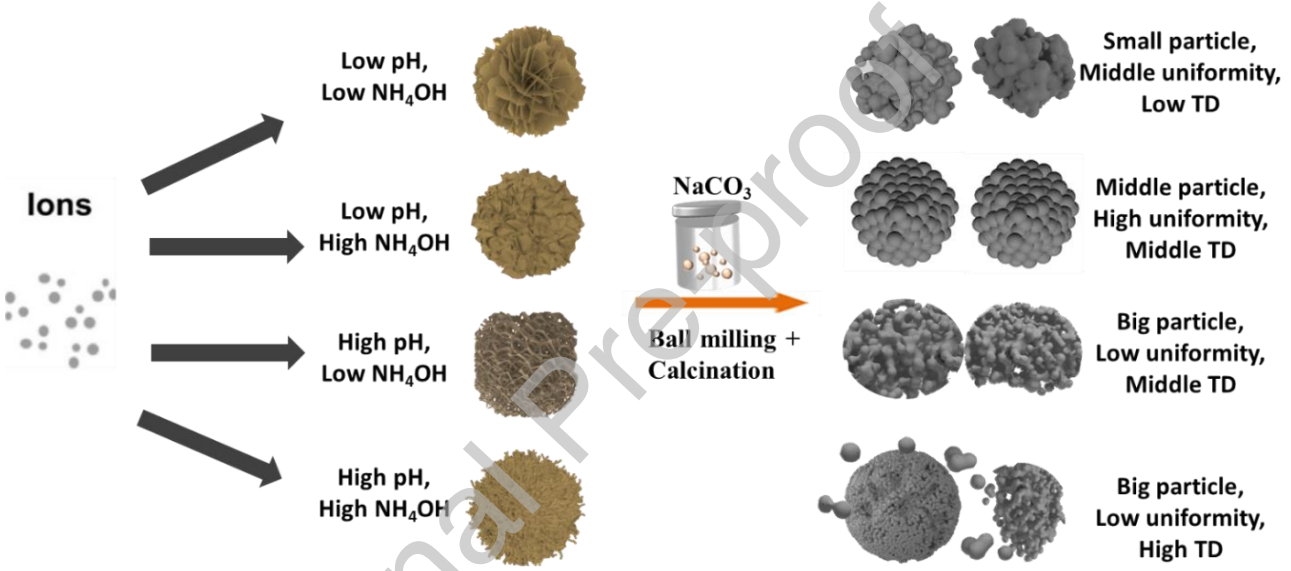

Figure 5. Schematic illustration of effects of synthetic factors on the precursor morphology and the physical properties of the final particles.

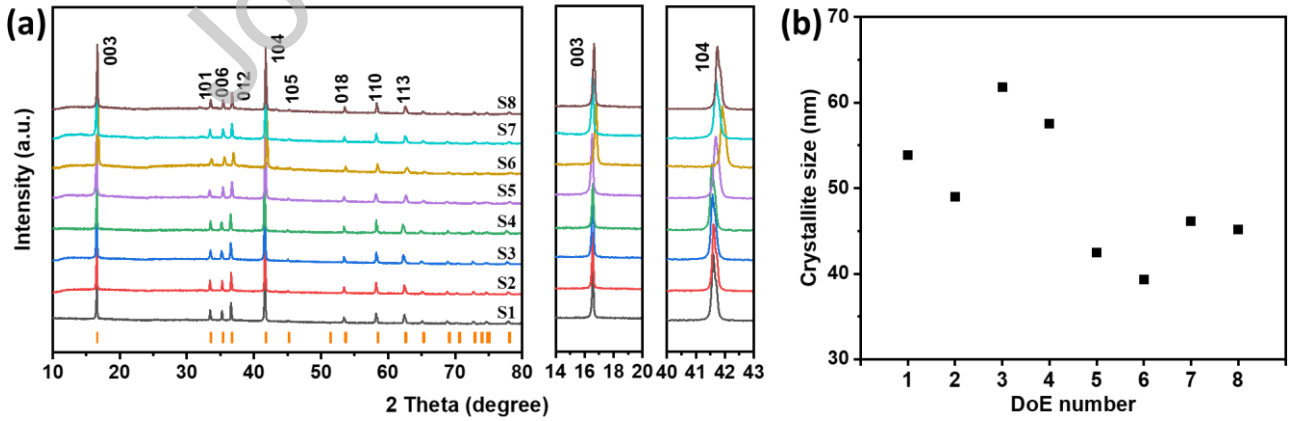

Figure 6. (a) XRD patterns of NaNFMO samples obtained under different conditions. (b) Crystallite size calculated from 003 and 104 peaks.

The XRD patterns (Fig. 6a) demonstrate the formation of single-phase materials in all cases, with indexing matching to a hexagonal O3-type α-$NaFeO_2$ structure (R-3m space group). However, upon closer examination of the (003) and (104) reflections, it can be observed that the diffraction peaks shift towards higher angles as the pH value increases. This shift indicates a contraction of the

interplanar spacing (c-axis). Rietveld refinements were conducted by using the GSAS software (Figure S1, S2), and the calculated lattice parameters are provided in Table S1. As shown in Figure S2, samples prepared by DoE 4 and DoE 6 exhibit the smallest values for lattice c and d003 spacing, which may lead to sluggish sodium ion diffusion and a decrease in electrochemical performance.

Additionally, an increase in the stirring speed, as seen in DOE5-8, leads to broadening of the diffraction peaks, indicating a decrease in crystallinity. The average crystal sizes for all samples were determined using the well-established Scherrer equation.

$$D=k\lambda/\beta\cos\theta \qquad (3)$$

Where K is a constant related to crystallite shape, normally taken as 0.94, λ is the X-ray wavelength in nanometer (nm), β is the peak width of the diffraction peak profile at half maximum height (FWHM) and θ is half the diffraction angle[30]. The calculation results show that the average crystal sizes decreased after increasing the stirring speed (Fig. 6b), which suggests that faster stirring may alter the surface properties, growth kinetics, and final morphology of NaNFMO.

3.2 Electrochemical properties

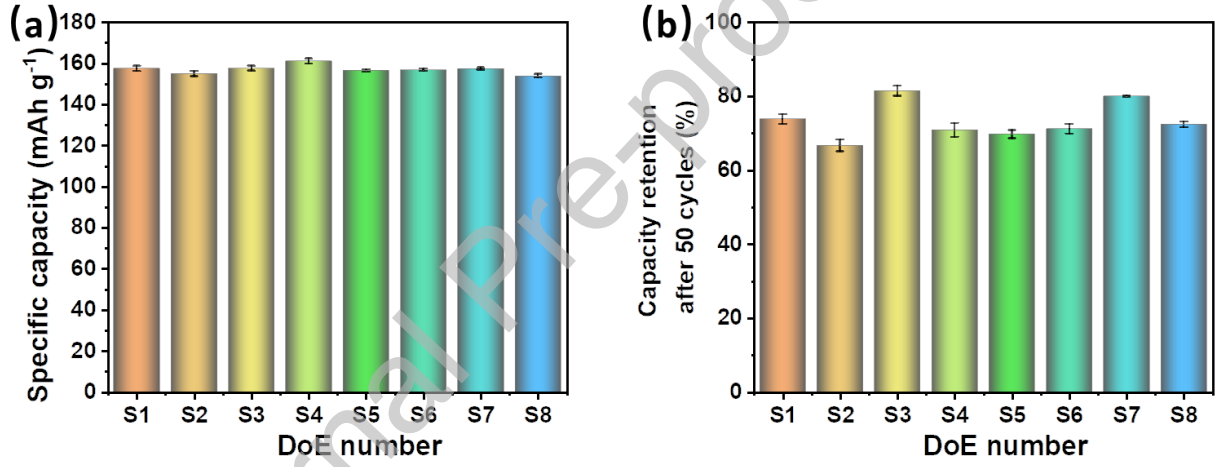

Figure 7. Formation capacity (a) and capacity retention after 50 cycles (b) for the as-synthesized materials.

The formation charge/discharge curves and the corresponding formation capacity (the 1st cycle) of the prepared cells with a current density of 15 mA g^{-1} (0.1C) are shown in Fig S3 and Fig 7a. The formation capacity varies slightly between 154.1 and 161.3 mAh g^{-1} with input parameters, and sample 8 synthesized pH=11, NH_4OH /$TMSO_4$=1.2, 800rpm shows the lowest initial capacity.

By contrast, significant variations were observed in terms of capacity retentions after 50 cycles at 0.5 C as shown in Figure 7b. Samples synthesized at lower pH value (10) tend to show better cycling performance than the ones synthesized at pH=11, and samples synthesized at pH=10, NH_4OH /$TMSO_4$=1.2 (S3, S7) give the highest capacity retentions. In addition, the significant difference in the vertical error bars is worth noting. Samples synthesized at low stirring speeds showed larger error bars in terms of both initial capacity and cycling stability, which may originate from the inhomogeneous distribution of the particles as shown in Fig 3-4. Therefore, higher stirring speed is preferred in terms of homogeneity.

O3-type layered oxides typically suffer from irreversible structural evolution upon Na^+ extraction /insertion process, which affects the cycling stability. Figure S4 gives the calculated dQ/dV vs. voltage plots from the first 3 cycles, where the plateau around 3.0 V (vs Na^+/Na) is related to the reversible phase transition from O3 to P3, and plateaux around 4.0 V (vs Na^+/Na) is associated with

the irreversible phase conversion of P3-P3' [31]. However, the cycling stability is not fully explained by crystal structure only, as shown in Figure S5, where the capacity retention is poorly related to either the capacity contribution from the different phases (A/B) or I003/I104, as indicated by the R^2. The weak relationship between cycling performance and structural properties indicates that capacity degradation is the result of a combination of intrinsic structural decay and extrinsic interface decay, which is closely related to the physical properties of the particles.

Table 3 Summary of experimental design and measured electrochemical response results.

DOE No.	Synthesis conditions			Response	
	pH	NH_4OH/ TM	Stirring speed (rpm)	Formation capacity (mAh g^{-1})	Capacity retention (%)
1	10.0	0.8	400	157.7	73.9
2	11.0	0.8	400	155.1	66.7
3	10.0	1.2	400	157.8	81.5
4	11.0	1.2	400	161.4	69.8
5	10.0	0.8	800	156.7	71.3
6	11.0	0.8	800	157.1	71.0
7	10.0	1.2	800	157.6	80.1
8	11.0	1.2	800	154.1	72.5
9	10.5	1.0	600	153.8	73.2
10	10.5	1.0	600	154.1	74.6
11	10.5	1.0	600	154.9	73.8

3.3 Response analysis and results of ANOVA

To quantify the impact of synthesis inputs on the physical and electrochemical outputs, factorial regressions were conducted to identify significant factors, determine coefficient effects, and generate regression equations using forward selection based on p-values (<0.05).

Figure 8 presents the Pareto chart illustrating the effective parameters for the regression models. The fitting results, including coded coefficients and corresponding confidence values, for the selected responses are presented in Table 4. Strong correlations were observed between input factors and particle size (D50), as evidenced by high R^2 and R^2_{pred} values. The R^2 values for tap density, crystallite size, and capacity retention were also notably high (around 0.95), although the R^2_{pred} values slightly decreased to around 0.9. Nevertheless, these values remain above the critical threshold of 0.8, indicating that the models can still be used for prediction [32]. Conversely, the

correlation function for I003/104 was less reliability, as indicated by the lower R^2_{pred} value. In addition, the influence of synthesis inputs on particle distribution and formation capacity was not clear and therefore they were not considered further in the analysis.

Based on the findings presented in Figure 8 and Table 4, it was determined that both the pH and NH_4OH amount are significant operating parameters that have an impact on particle size (D50) and capacity retention. In contrast, the influence of stirring speed is relatively less pronounced within the constrained operating region. However, the interaction effects of pH with NH_4OH or stirring speed were found to be significant. Additionally, both tap density and crystallite size were found to be influenced by all three parameters. Notably, NH_4OH concentration exhibited the most significant influence on tap density, whereas stirring speed had the strongest impact on crystallite size.

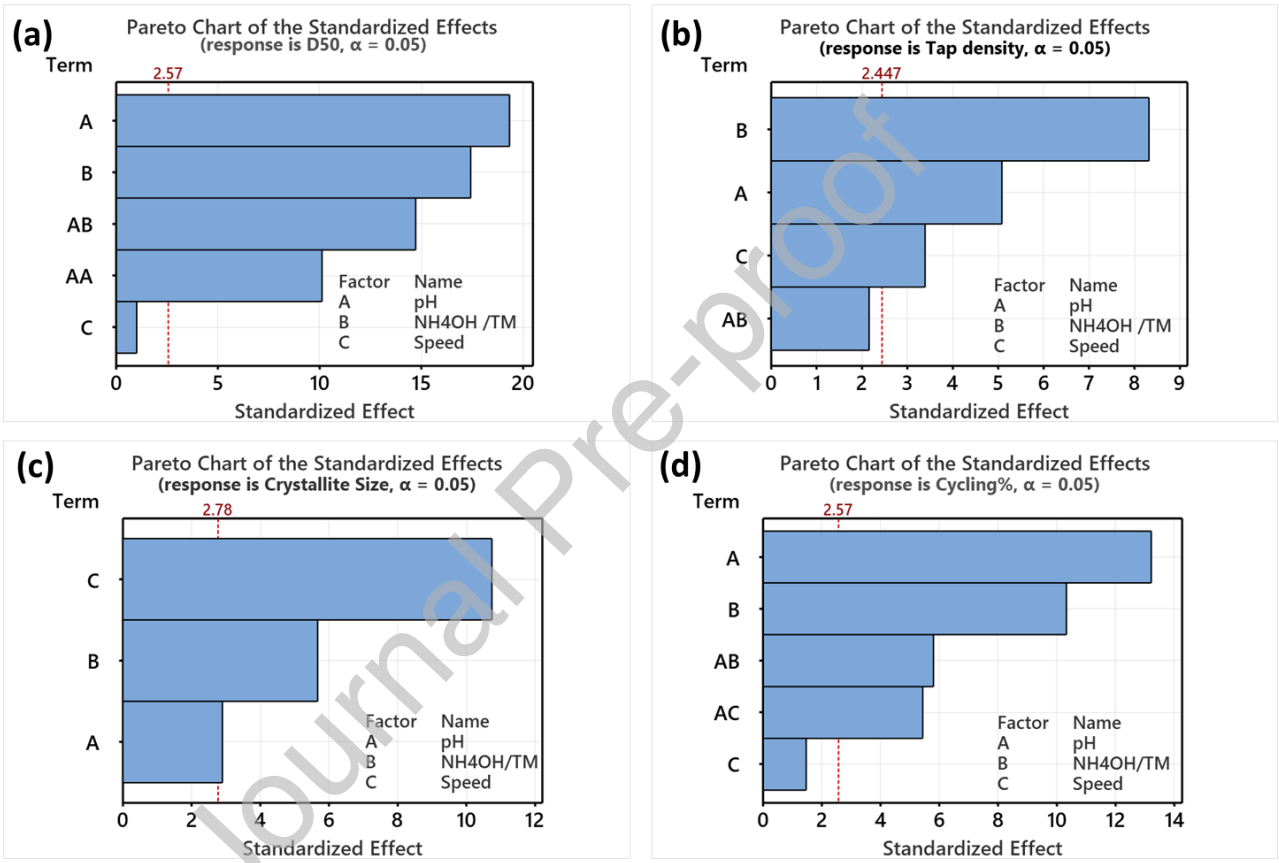

Figure 8. Pareto charts of effective parameters for the regression model (a) Particle size D50, (b) Tap Density, (c) Crystallite Size, and (d) Capacity Retention.

Table 4 Summary of fitted models with coded coefficients and corresponding confidence levels for the prediction of the selected responses (β_1 for pH, β_2 for NH_4OH/TM, β_1 for speed).

	Response				
Coefficients (in Coded Units	**Particle size D50**	**Tap density**	**Crystallize size**	**I003/I104**	**Capacity retention**
β_0	2.210	1.2091	49.412	0.9358	73.494
β_1	2.681	0.0825	-1.658	--	-3.354
β_2	2.416	0.1350	3.245	--	2.621
β_3	0.139	0.0550	-6.148	0.1032	0.371
β_{12}	2.041	0.0350	--	--	-1.471

β_{13}	--	--	--	--	1.379
β_{23}	--	--	--	--	--
β_1^2	2.686	--	--	--	--
$\mathbf{R^2}$	0.9942	0.9488	0.9750	0.8298	0.9858
$\mathbf{R^2_{pred}}$	0.9643	0.8648	0.8999	0.6974	0.9101

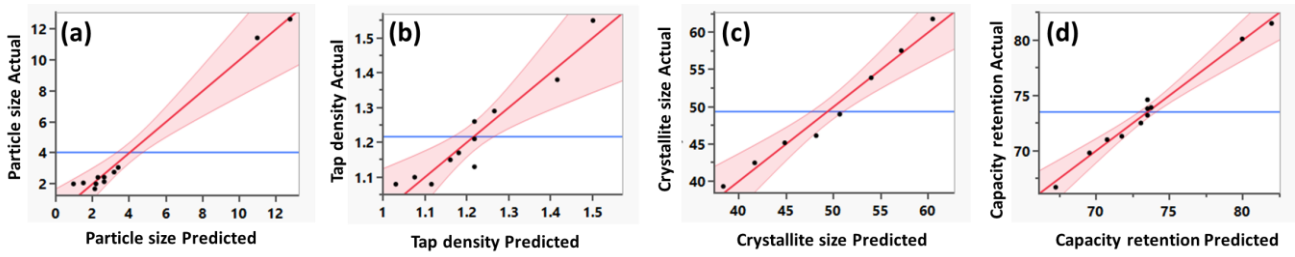

Figure 9 The distribution of the predicted *versus* actual values of the Particle size D50 (a), Tap Density (b), Crystallite Size (c), and Capacity Retention (d).

To assess the accuracy of the regression models, the comparison between the experimental results and the predicted values obtained from the fitted models is presented in Figure 9. The actual experimental values from the designed DoE runs are depicted as black dots, while the red straight line represents the ideal prediction. The graph demonstrates that the experimental values closely align with the prediction line and exhibit a normal distribution. This indicates that the fitted models accurately represent the selected responses.

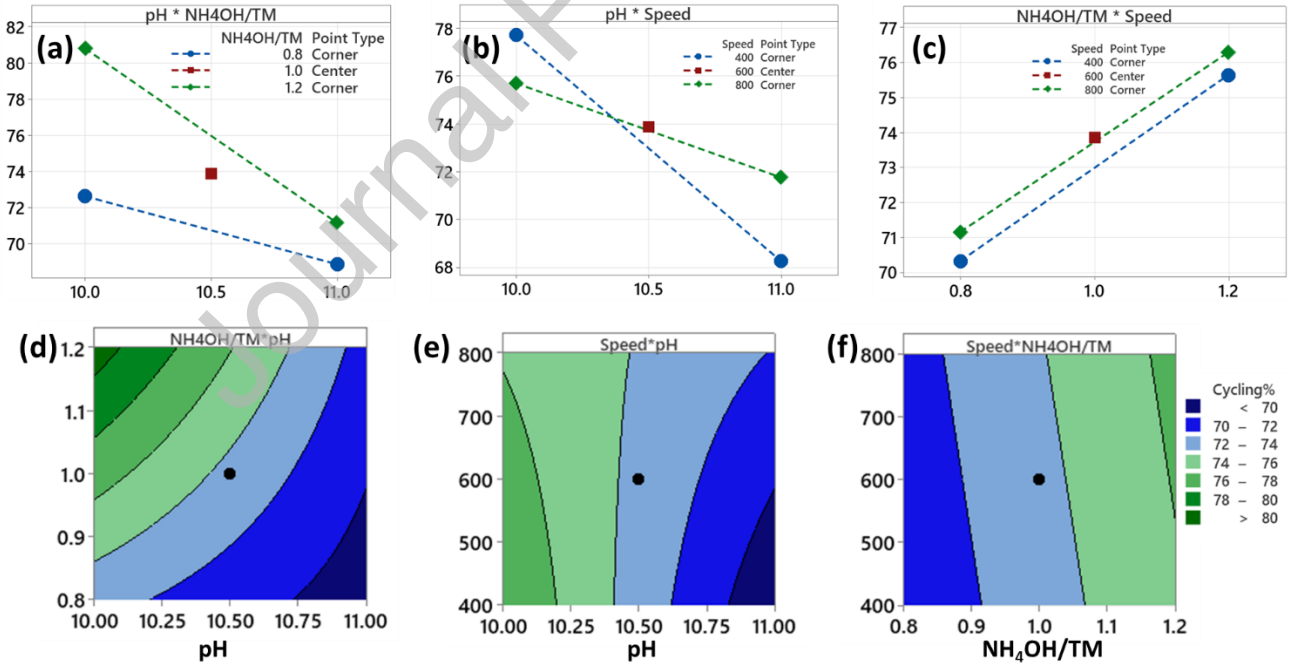

Figure 10 Interaction effect plots (a-c) and corresponding contour plots (d-f) for capacity retention.

To provide further information upon the impact of input factors on output responses, interaction contour plots depicting the relationship between factors and responses are presented in Figure 10 and Figure S6-8. Among the various output responses, capacity retention is chosen as a representative example for detailed discussion.

The interaction effect plots, and corresponding contour plots of the cycling performance are shown in Figure 10. These plots illustrate the relationship between pH and NH_4OH (Figure 10a, d), pH and speed (Figure 10b, e), and NH_4OH and speed (Figure 10c, f). By analyzing the interaction effects of different synthesis parameters on the cycling performance, optimal synthesis conditions can be determined. According to the ANOVA results presented in Table 4, the pH* NH_4OH interaction is identified as the most significant second-order interaction. When the pH value is increased from 10 to 11 at a high level of NH_4OH (green line in Fig. 10a), the cycling retention drops rapidly. However, the negative effect of pH is less pronounced at the low level of NH_4OH. The capacity retention decreases by 5.19% and 11.94% at the low and high levels of NH_4OH, respectively. The contour plot (Fig. 10d) reveals that the highest cycling retention is achieved within a narrow region, specifically for pH values ranging from 10.0 to 10.1 and NH_4OH levels ranging from 1.15 to 1.2.

The interaction of pH*speed is another important factor to consider. In Figure 10b, two lines intersect at around pH=10.4, indicating that below this pH value, materials produced with lower stirring speed exhibit longer cycle life. This can be attributed to the decrease in solution supersaturation at low pH, which promotes particle growth rather than nucleation. Higher energy stirring, on the other hand, may crush the immature particles, negatively affecting particle growth. This observation is consistent with the samples from DoE1 and DoE5 shown in Figure 3a and e. In contrast, at higher pH, solution supersaturation increases, leading to higher nucleation rates. Higher energy stirring enhances the collision between primary particles, facilitating particle agglomeration and growth. The optimal pH*speed setting can be determined as $10.0 \leq pH \leq 10.2$ and $400 \leq speed \leq 750$, as depicted in the contour plot (Figure 10e).

The NH_4OH*speed interaction plots (Figure 10c, f) indicate that the cycling performance is not significantly influenced by the stirring speed. However, there is an increasing trend in better cycling performance as the level of NH_4OH is increased.

Based on the analysis above, the optimal conditions for achieving the highest cycling performance are: $10.0 \leq pH \leq 10.1$, $1.15 \leq NH_4OH/Metal \leq 1.2$, $400 \leq Speed \leq 750$. Although the effect of stirring speed is less pronounced within the range studied, a higher stirring speed can lead to a narrower particle size distribution resulting in improved consistency in terms of initial capacity and cycling stability, as discussed earlier. Therefore, an intermediate value of speed (600 rpm) was chosen for the subsequent experiments.

4. VALIDATION EXPERIMENTS

To validate the optimal synthetic conditions determined through the above analysis, a confirmatory experiment was conducted using the selected settings: pH= 10.1, NH_4OH/Metal ratio of 1.2, and stirring speed of 600 rpm.

Figure 11 shows the SEM images of $Ni_{1/3}Fe_{1/3}Mn_{1/3}(OH)_2$ and $NaNi_{1/3}Fe_{1/3}Mn_{1/3}O_2$ synthesized using optimal parameters. Throughout the process, the precursor was collected at various time intervals to monitor the growth of particle size and morphology. After 2 hours, secondary particles were observed, resulting from the agglomeration of loosely packed primary particles. Over time, the agglomerates became more compacted, and the particle sizes gradually increased. The particles also exhibited a more spherical shape with a smoother surface. After 24 hours, a flower-like secondary particle composed of lamellar primary particles, measuring approximately 400 nm in lateral dimension, was observed. In Figure 11 g the morphology of $NaNi_{1/3}Fe_{1/3}Mn_{1/3}O_2$ after sodiation is shown. The lamellar primary particles transformed into thick plate shapes, and spherical second particles with a narrow size distribution were obtained, as shown in the particle

size distribution diagram (Figure 11h). The relatively dense packing and uniform size distribution contribute to a high tap density of 1.50 g cm^{-3}.

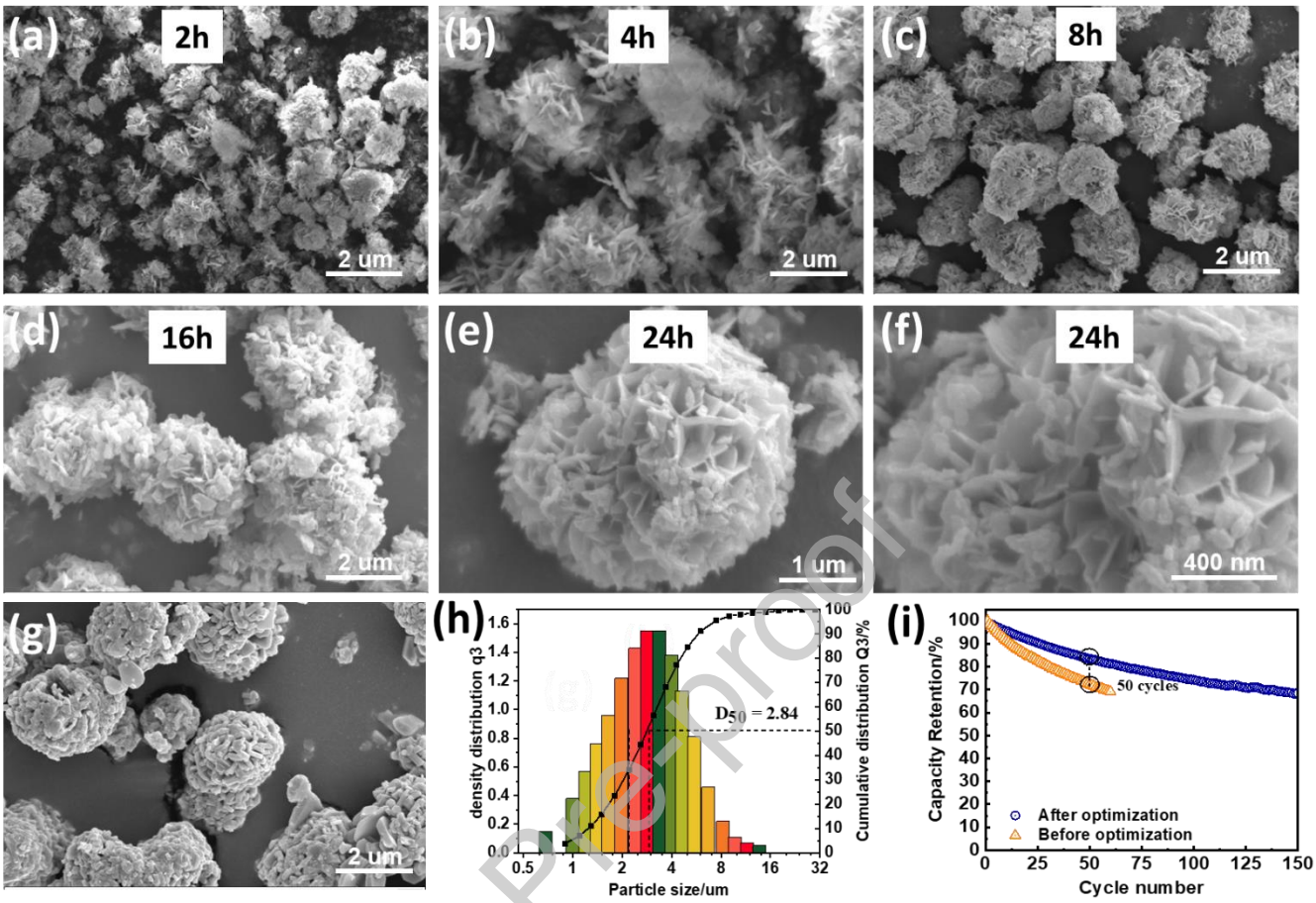

Fig. 11. (a-f) SEM images of $Ni_{1/3}Fe_{1/3}Mn_{1/3}(OH)_2$ collected at different reaction time. SEM image (g) and Particle size distribution (h) of Na $Ni_{1/3}Fe_{1/3}Mn_{1/3}O_2$ synthesized under optimized conditions. (i) Comparison of cycling performance before and after optimization.

Figure 11i shows the cycling performance of optimized $NaNi_{1/3}Fe_{1/3}Mn_{1/3}O_2$. After 50 cycles at 0.5C, the capacity retention reaches 83.43%, which is higher compared to the sample synthesized using the central point parameters prior to optimization. Table 5 provides a summary comparison of the selected responses, including both experimental and predicted values obtained from the empirical models. The results demonstrate good agreement between the predicted and experimental values, with a deviation of less than 10% for all selected responses. The improved cycling performance, coupled with the validation of the empirical models, serves as evidence of the success achieved through the DoE optimization process.

Table 5 Comparison of experimental and predicted values for selected responses

Response	Experimental value	Predicted value	Deviation
Particle size D50/um	2.84	2.65	6.69%
Tap density/ g cm^{-3}	1.35	1.25	7.41%
Crystallize size/nm	56.72	53.98	4.83%
Capacity retention/%	83.43	79.97	4.15%

It is important to acknowledge that this study focused on the investigation of three selected factors. However, further research is warranted to explore the influence of additional parameters such as residence time, feeding concentration, and feeding flow rate. Additionally, a subsequent experimental design within a smaller design space, utilizing the response surface method (RSM), would be beneficial for a more comprehensive evaluation of the effects of pH and NH_4OH, as well as their interactions on the physiochemical properties of $NaNi_{1/3}Fe_{1/3}Mn_{1/3}O_2$ cathode materials.

5. CONCLUSIONS:

Sodium nickel iron manganese oxide ($NaNi_{1/3}Fe_{1/3}Mn_{1/3}O_2$) cathode materials for sodium-ion batteries were synthesized using a hydroxide coprecipitation process. The physical properties and electrochemical performance of the synthesized materials were investigated in relation to three process variables: pH, the molar ratio of NH_4OH/MSO_4, and stirring speed. A statistical experimental design method was employed to identify the key factors and develop regression models to predict the optimised synthesis conditions for long cycle life.

Four regression equations were derived to describe the relationship between the synthesis factors and the selected responses, D50 (particle size), tap density, crystallite size, and capacity retention. These equations provided valuable insights into how the synthesis conditions influence the physical properties of the particles and their electrochemical performance.

The analysis revealed that both pH and NH_4OH significantly affect all the selected responses. Higher pH values result in larger secondary particle sizes (D50) and higher tap densities, but lead to decreased crystallite sizes and particle uniformity, ultimately impacting the cycling performance. Higher NH_4OH concentration played a positive role in all the studied particle properties, contributing to improved uniformity and tap density. Stirring speed, while less pronounced overall, emerged as a significant factor for crystallite size. The interaction effects of pH with NH_4OH or stirring speed were also found to be significant in determining the final cycling performance.

Based on the experimental design method, the optimal synthesis conditions for achieving the best cycling performance were determined to be within the ranges of $10.0 \leq pH \leq 10.1$, $1.15 \leq NH_4OH/Metal \leq 1.2$, and $400 \leq Speed \leq 750$. A confirmatory experiment conducted under these optimized conditions results in particles with uniform size distribution and a high tap density of 1.50 g cm^{-3}. This improvement in particle characteristics contributed to significantly improved cycle-life performance compared to the pre-optimization state. Whilst this study was performed with a sodium-ion Iron, manganese, nickel mixed oxide, the same principles can be utilised for other sodium and lithium-ion cathode materials.

This work shows that through careful optimisation of the synthesis conditions, we can inform the design of these layered oxide cathode materials and improve the performance properties including cycle life. This allows us to tailor the materials for high energy density and cycle life for stationary storage applications.

Acknowledgements

We acknowledge the funding support received from Faraday Institution (faraday.ac.uk; EP/S003053/1), Multiscale Modelling Project (FIRG025), Nextrode (FIRG015), CATMAT (FIRG016).

Data Availability

The raw data and processed data required to reproduce these findings are available to download from [https://data.mendeley.com/datasets/gxvxdz7ys3/draft?a=2e3ef0bb-0bde-4478-bcf1-3682c1194240].

REFERENCES

1. Wadia, C., P. Albertus, and V. Srinivasan, *Resource constraints on the battery energy storage potential for grid and transportation applications.* Journal of Power Sources, 2011. **196**(3): p. 1593-1598.
2. Grosjean, C., et al., *Assessment of world lithium resources and consequences of their geographic distribution on the expected development of the electric vehicle industry.* Renewable and Sustainable Energy Reviews, 2012. **16**(3): p. 1735-1744.
3. Speirs, J., et al., *The future of lithium availability for electric vehicle batteries.* Renewable and Sustainable Energy Reviews, 2014. **35**: p. 183-193.
4. Olivetti, E.A., et al., *Lithium-Ion Battery Supply Chain Considerations: Analysis of Potential Bottlenecks in Critical Metals.* Joule, 2017. **1**(2): p. 229-243.
5. *Net Zero by 2050 A Roadmap for the Global Energy Sector.* 2021.
6. Vaalma, C., et al., *A cost and resource analysis of sodium-ion batteries.* Nature Reviews Materials, 2018. **3**(4).
7. Goikolea, E., et al., *Na - Ion Batteries–Approaching Old and New Challenges.* Advanced Energy Materials, 2020.
8. Harper, G.D.J., et al., *Roadmap for a sustainable circular economy in lithium-ion and future battery technologies.* Journal of Physics: Energy, 2023. **5**(2).
9. Patrick T. Moseley, D.A.J.R., *High-Temperature Sodium Batteries for Energy Storage.* Electrochemical Energy Storage for Renewable Sources and Grid Balancing, 2015: p. 253-268.
10. Hirsh, H.S., et al., *Sodium - Ion Batteries Paving the Way for Grid Energy Storage.* Advanced Energy Materials, 2020. **10**(32).
11. Ellis, B.L. and L.F. Nazar, *Sodium and sodium-ion energy storage batteries.* Current Opinion in Solid State and Materials Science, 2012. **16**(4): p. 168-177.
12. Roberts, S. and E. Kendrick, *The re-emergence of sodium ion batteries: testing, processing, and manufacturability.* Nanotechnol Sci Appl, 2018. **11**: p. 23-33.
13. al, K.S.e., *<'Novel High Energy Density Sodium Layered Oxide Cathode Materials_ from Material to Cells'.pdf>.* K.Smith, J.Treacher, D. Ledwoch, P. Adamson, and E.Kendrick, Novel High Energy Density Sodium Layered Oxide Cathode Materials : From Material to Cells. ECS Transactions, 2017, 75 (22). p. 13-24., 2017.
14. Pasta, M., et al., *Full open-framework batteries for stationary energy storage.* Nat Commun, 2014. **5**: p. 3007.
15. Kim, D., et al., *Layered Na[Ni1/3Fe1/3Mn1/3]O2 cathodes for Na-ion battery application.* Electrochemistry Communications, 2012. **18**: p. 66-69.
16. Yu, Y., et al., *Revealing the anionic redox chemistry in O3-type layered oxide cathode for sodium-ion batteries.* Energy Storage Materials, 2021. **38**: p. 130-140.
17. Zhang, Q., et al., *F-doped O3-NaNi1/3Fe1/3Mn1/3O2 as high-performance cathode materials for sodium-ion batteries.* Science China Materials, 2017. **60**(7): p. 629-636.
18. Jeong, M., et al., *O3-type NaNi1/3Fe1/3Mn1/3O2 layered cathode for Na-ion batteries: Structural evolution and redox mechanism upon Na (de) intercalation.* Journal of Power Sources, 2019. **439**.
19. Wang, H., et al., *Large-Scale Synthesis of NaNi1/3Fe1/3Mn1/3O2as High Performance Cathode Materials for Sodium Ion Batteries.* Journal of The Electrochemical Society, 2016. **163**(3): p. A565-A570.
20. Li, X., et al., *O3-NaFe(1/3-x)Ni1/3Mn1/3AlxO2 Cathodes with Improved Air Stability for Na-Ion Batteries.* ACS Appl Mater Interfaces, 2021.
21. Mu, L., et al., *Surface transformation by a "cocktail" solvent enables stable cathode materials for sodium ion batteries.* Journal of Materials Chemistry A, 2018. **6**(6): p. 2758-2766.
22. Liang, L., et al., *Co–precipitation synthesis of Ni0.6Co0.2Mn0.2(OH)2 precursor and characterization of LiNi0.6Co0.2Mn0.2O2 cathode material for secondary lithium batteries.* Electrochimica Acta, 2014. **130**: p. 82-89.
23. Lee, M.H., et al., *Synthetic optimization of Li[Ni1/3Co1/3Mn1/3]O2 via co-precipitation.* Electrochimica Acta, 2004. **50**(4): p. 939-948.
24. Noh, M. and J. Cho, *Optimized Synthetic Conditions of LiNi0.5Co0.2Mn0.3O2Cathode Materials for High Rate Lithium Batteries via Co-Precipitation Method.* Journal of The Electrochemical Society, 2012. **160**(1): p. A105-A111.
25. Barai, P., et al., *Multiscale Computational Model for Particle Size Evolution during Coprecipitation of Li-Ion Battery Cathode Precursors.* J Phys Chem B, 2019. **123**(15): p. 3291-3303.
26. Para, M.L., et al., *A modelling and experimental study on the co-precipitation of Ni0.8Mn0.1Co0.1(OH)2 as precursor for battery cathodes.* Chemical Engineering Science, 2022. **254**.
27. Hwang, B.J., et al., *A Combined Computational/Experimental Study on LiNi1/3Co1/3Mn1/3O2.* Chemistry of Materials, 2003. **15**(19): p. 3676-3682.
28. Cai, X., et al., *Understanding mechanism of voltage decay and temperature sensitivity of Li-rich manganese-based cathode materials.* Materials & Design, 2023. **225**.

29. van Bommel, A. and J.R. Dahn, *Analysis of the Growth Mechanism of Coprecipitated Spherical and Dense Nickel, Manganese, and Cobalt-Containing Hydroxides in the Presence of Aqueous Ammonia.* Chemistry of Materials, 2009. **21**(8): p. 1500-1503.
30. Monshi, A., M.R. Foroughi, and M.R. Monshi, *Modified Scherrer Equation to Estimate More Accurately Nano-Crystallite Size Using XRD.* World Journal of Nano Science and Engineering, 2012. **02**(03): p. 154-160.
31. Song, T., et al., *High-Voltage Stabilization of O3-Type Layered Oxide for Sodium-Ion Batteries by Simultaneous Tin Dual Modification.* Chemistry of Materials, 2022.
32. Myers, R.H., D.C. Montgomery, and C.M. Anderson-Cook, *Response Surface Methodology: Process and Product Optimization Using Designed Experiments*. 2011: Wiley.

Table 1 Experimental design matrix for the $Ni_{1/3}Fe_{1/3}Mn_{1/3}(OH)_2$ co-precipitation reactions with different pH, ammonium hydroxide quantity and stirring speed.

DOE No.	Uncoded			Coded		
	x_1 pH	x_2 NH_4OH/TM	x_3 Stirring speed (rpm)	x_1 pH	x_2 NH_4OH/TM	x_3 Stirring speed (rpm)
1	10.0	0.8	400	-1	-1	-1
2	11.0	0.8	400	1	-1	-1
3	10.0	1.2	400	-1	1	-1
4	11.0	1.2	400	1	1	-1
5	10.0	0.8	800	-1	-1	1
6	11.0	0.8	800	1	-1	1
7	10.0	1.2	800	-1	1	1
8	11.0	1.2	800	1	1	1
9	10.5	1.0	600	0	0	0
10	10.5	1.0	600	0	0	0
11	10.5	1.0	600	0	0	0

Table 2 Summary of experimental design and measured physical response results.

DOE No.	Synthesis conditions			Response				
	pH	NH_4OH/TM	Stirring speed (rpm)	Particle size D50 (um)	Size distribution	Tap density (g/cm^3)	Crystallite size (nm)	I003/I104
1	10.0	0.8	400	2.0	1.7	1.0	53.9	0.82
2	11.0	0.8	400	3.2	2.1	1.1	49.0	0.88
3	10.0	1.2	400	2.4	1.7	1.2	61.8	0.90
4	11.0	1.2	400	11.4	3.1	1.4	57.5	0.73
5	10.0	0.8	800	1.7	1.6	1.1	42.5	1.03
6	11.0	0.8	800	3.1	1.8	1.2	39.3	1.02
7	10.0	1.2	800	2.8	1.5	1.3	46.1	1.07
8	11.0	1.2	800	12.6	2.5	1.6	45.2	1.03
9	10.5	1.0	600	2.1	1.8	1.1	52.0	0.87
10	10.5	1.0	600	2.1	1.7	1.2	55.9	0.92
11	10.5	1.0	600	2.4	1.5	1.3	51.1	0.85

Table 3 Summary of experimental design and measured electrochemical response results.

DOE No.	Synthesis conditions			Response	
	pH	NH_4OH/ TM	Stirring speed (rpm)	Formation capacity (mAh g^{-1})	Capacity retention (%)
1	10.0	0.8	400	157.7	73.9
2	11.0	0.8	400	155.1	66.7
3	10.0	1.2	400	157.8	81.5
4	11.0	1.2	400	161.4	69.8
5	10.0	0.8	800	156.7	71.3
6	11.0	0.8	800	157.1	71.0
7	10.0	1.2	800	157.6	80.1
8	11.0	1.2	800	154.1	72.5
9	10.5	1.0	600	153.8	73.2
10	10.5	1.0	600	154.1	74.6
11	10.5	1.0	600	154.9	73.8

Table 4 Summary of fitted models with coded coefficients and corresponding confidence levels for the prediction of the selected responses (β_1 for pH, β_2 for NH_4OH/TM, β_3 for speed).

	Response				
Coefficients (in Coded Units	**Particle size D50**	**Tap density**	**Crystallize size**	**I003/I104**	**Capacity retention**
β_0	2.210	1.2091	49.412	0.9358	73.494
β_1	2.681	0.0825	-1.658	--	-3.354
β_2	2.416	0.1350	3.245	--	2.621
β_3	0.139	0.0550	-6.148	0.1032	0.371
β_{12}	2.041	0.0350	--	--	-1.471
β_{13}	--	--	--	--	1.379
β_{23}	--	--	--	--	--
β_1^2	2.686	--	--	--	--
R^2	0.9942	0.9488	0.9750	0.8298	0.9858
R^2_{pred}	0.9643	0.8648	0.8999	0.6974	0.9101

Table 5 Comparison of experimental and predicted values for selected responses

Response	Experimental value	Predicted value	Deviation
Particle size D50/um	2.8	2.6	7.7%
Tap density/ g cm^{-3}	1.5	1.3	15.4%
Crystallize size/nm	56.7	54.0	5.4%
Capacity retention/%	83.4	80.0	4.3%

We acknowledge the funding support received from Faraday Institution (faraday.ac.uk; EP/S003053/1), Multiscale Modelling Project (FIRG025), Nextrode (FIRG015), CATMAT (FIRG016), NEXGENNA FIRG064

Declaration of interests

☒The authors declare that they have no known competing financial interests or personal relationships that could have appeared to influence the work reported in this paper.

☐The authors declare the following financial interests/personal relationships which may be considered as potential competing interests: